SCIENCE CHINA Materials ARTICLES

mater.scichina.com link.springer.com

Published online 25 August 2020 | https://doi.org/10.1007/s40843-020-1437-2
Sci China Mater 2021, 64(2): 307–317

Carbon-coated Fe_2O_3 hollow sea urchin nanostructures as high-performance anode materials for lithium-ion battery

Yuge Feng[1], Na Shu[2], Jian Xie[2], Fei Ke[3], Yanwu Zhu[2] and Junfa Zhu[1*]

ABSTRACT **Fe_2O_3 has become a promising anode material in lithium-ion batteries (LIBs) in light of its low cost, high theoretical capacity (1007 mA h g^{-1}) and abundant reserves on the earth. Nevertheless, the practical application of Fe_2O_3 as the anode material in LIBs is greatly hindered by several severe issues, such as drastic capacity falloff, short cyclic life and huge volume change during the charge/discharge process. To tackle these limitations, carbon-coated Fe_2O_3 (Fe_2O_3@MOFC) composites with a hollow sea urchin nanostructure were prepared by an effective and controllable morphology-inherited strategy. Metal-organic framework (MOF)-coated FeOOH (FeOOH@-MIL-100(Fe)) was applied as the precursor and self-sacrificial template. During annealing, the outer MOF layer protected the structure of inner Fe_2O_3 from collapsing and converted to a carbon coating layer *in situ*. When applied as anode materials in LIBs, Fe_2O_3@MOFC composites showed an initial discharge capacity of 1366.9 mA h g^{-1} and a capacity preservation of 1551.3 mA h g^{-1} after 200 cycles at a current density of 0.1 A g^{-1}. When increasing the current density to 1 A g^{-1}, a reversible and high capacity of 1208.6 mA h g^{-1} was obtained. The enhanced electrochemical performance was attributed to the MOF-derived carbon coating layers and the unique hollow sea urchin nanostructures. They mitigated the effects of volume expansion, increased the lithium-ion mobility of electrode, and stabilized the as-formed solid electrolyte interphase films.**

Keywords: lithium-ion battery, transition metal oxide, MOF-derived carbon, anode, hollow sea urchin nanostructures

INTRODUCTION

Lithium-ion batteries (LIBs) have been widely used as electrochemical energy storage devices [1,2]. With more rigorous requirements for improved electrochemical energy storage devices, it is essential to develop safe and low-cost LIBs with high power density and long lifetime [3,4].

Transition metal oxides (TMOs) are promising anode materials for LIBs due to their higher theoretical capacities (500–1000 mA h g^{-1}) than conventional graphite electrode (372 mA h g^{-1}) [5,6]. Among various TMOs, Fe_2O_3 is the most attractive anode material for LIBs, because of its low cost and high theoretical capacity (1007 mA h g^{-1}) [7]. However, some serious issues limit its practical application in LIBs. For example, slow transmission of lithium ions and electrons in active substances results in poor rate performance [8,9]. Another severe problem is dramatic capacity fading, which is caused by the formation of irreversible solid electrolyte interphase (SEI), harsh aggregation and huge volume change during the charge/discharge process [10–12]. Various efforts have been made to tackle these problems: one could coat or hybridize iron oxide materials with advanced carbon matrix and construct unique structures which can shorten the ionic diffusion distance, relieve the volume change efficiently and increase the area between the electrolyte and active materials [13–17].

Metal-organic frameworks (MOFs) are crystalline materials consisting of organic ligands and transition metal ions/clusters [18–21]. They have shown prominent performances in many fields, arising from their large surface areas and tunable framework-like architectures [22–25]. Inheriting the high surface areas, uniform active het-

[1] National Synchrotron Radiation Laboratory, Department of Chemical Physics and Key Laboratory of Surface and Interface Chemistry and Energy Catalysis of Anhui Higher Education Institutes, University of Science and Technology of China, Hefei 230029, China
[2] Hefei National Research Center for Physical Science at the Microscale CAS Key Laboratory of Materials for Energy Conversion & Department of Materials Science and Engineering, University of Science and Technology of China, Hefei 230026, China
[3] Department of Applied Chemistry and State Key Laboratory of Tea Plant Biology and Utilization, Anhui Agricultural University, Hefei 230026, China
[*] Corresponding author (email: jfzhu@ustc.edu.cn)

eroatom doping and well-defined porous structure of MOFs, their derivative porous carbon composites have broad applications in LIBs [26]. For example, Lou's group [9] used Prussian blue $Fe_4[Fe(CN)_6]_3$ as a precursor and self-sacrificial template to synthesize Fe_2O_3 microboxes. Yi *et al.* [27] also applied a similar method to prepare bimetallic nickel cobalt sulfide and nitrogen-doped carbon hollow spherical structures through direct calcination of MOFs (Ni–Co–BTC–n). Hou *et al.* [28] reported a one-dimensional (1D) porous rod-like structured carbon-coated Cu–Co bimetal oxide composite material, ($Cu_xCo_{3-x}O_4$/C), which was prepared through a morphology-inherited pyrolysis of MOFs (Cu–Co–BTC). All of these MOF-derived materials exhibited excellent anode performances. However, to our knowledge, only few studies of MOF-derived porous carbon composites have been reported as carbon coatings of metal oxides with unique structure applied in LIBs [29].

Here, we developed a concise and controllable approach for preparation of Fe_2O_3 hollow sea urchin nanostructures coated with MOF-derived carbon composites (Fe_2O_3@MOFC). MOFs were applied as self-sacrificial templates for the *in-situ* growth of carbon coating composites. It is found that these carbon coating layers not only enhanced the LIBs property of electrode materials, but also helped to stabilize the structure of Fe_2O_3 during the charge/discharge process. The as-prepared Fe_2O_3@MOFC hollow sea urchin nanostructures exhibited enhanced cycling performance (1577 mA h g^{-1} after 200 cycles at 0.1 A g^{-1} and 1171 mA h g^{-1} after 300 cycles at 1 A g^{-1}) and excellent rate performance.

EXPERIMENTAL SECTION

Synthesis of FeOOH

$FeSO_4{\cdot}7H_2O$ (0.111 g) was dissolved in a solution of 35 mL deionized water and 5 mL glycerol. After magnetic stirring for 10 min, the solution was decanted to a Teflon-lined stainless steel autoclave and then heated at 120°C for 24 h. The collected precipitates were washed with deionized water and ethanol and then dried at 60°C for 12 h.

Synthesis of FeOOH@MIL-100(Fe)

FeOOH nanoparticles were functionalized with mercaptoacetic acid (MAA). After that, 0.01 g MAA-functionalized FeOOH was dispersed in 4 mL $FeCl_3{\cdot}6H_2O$ ethanol solution (10 mmol L^{-1}) for 15 min and then in 4 mL benzene-1,3,5-tricarboxylic acid (H_3BTC) ethanol solution (10 mmol L^{-1}) at 70°C for 30 min. Between each step, the nanoparticles were washed with ethanol. After ten cycles, the samples were recovered and washed with ethanol, and then dried under vacuum at 60°C.

Synthesis of MIL-100(Fe) MOF materials

$FeCl_3{\cdot}6H_2O$ (10 mmol L^{-1}, 20 mL) ethanol solution was added to 20 mL H_3BTC (10 mmol L^{-1}) ethanol solution. After magnetic stirring for 10 min, the mixture was transferred into a Teflon-lined stainless steel autoclave and then heated at 120°C for 1 h. After that, the product was placed in a drying oven for 12 h to remove the solvent.

Synthesis of Fe_2O_3@MOFC, Fe_2O_3 and MOFC

The FeOOH@MIL-100(Fe), FeOOH and MOFs were annealed in a nitrogen atmosphere at 600°C for 5 h. The heating rate was 1°C min^{-1}. Then the samples were cooled down to room temperature. Fe_2O_3@MOFC composites, Fe_2O_3 and MOFC were obtained, respectively.

Characterization

X-ray diffraction (XRD) patterns were measured on a Philips X' pert Pro Super diffractometer with Cu Kα radiation (λ = 1.54 Å). The surface areas were evaluated with the Brunauer-Emmett-Teller (BET) method (Micromeritics TriStar II 3020). Raman spectra were measured with a Renishaw inVia Raman Microscope. Transmission electron microscopy (TEM) images were obtained with a JEOL-2100F transmission electron microscope. Scanning electron microscopy (SEM) measurements were carried out on a JSM-6700F scanning electron microscope. X-ray photoelectron spectra (XPS) were carried out at the Catalysis and Surface Science end-station of the National Synchrotron Radiation Laboratory (NSRL), University of Science and Technology of China (USTC). The photon energies for Fe 2p, O 1s and C 1s were selected to be 1486.4, 600 and 350 eV, respectively. The synchrotron radiation soft X-ray microscopy images were obtained at the beamline BL07W in NSRL, USTC.

Lithium-ion battery measurements

The electrochemical performances of Fe_2O_3@MOFC, Fe_2O_3 and MOFC were tested using CR2016 coin-type cells. To prepare the Fe_2O_3@MOFC working electrode, aqueous slurry containing Fe_2O_3@MOFC composites (80 wt%), polyvinylidene fluoride (PVDF) binder (10 wt%), and conductive super-P carbon black (10 wt%) were pasted onto the surface of a copper foil and then dried under vacuum at 80°C for 12 h. Then the coin-type cells were assembled in an argon-filled glove-box. For

LIBs, metallic lithium foils were used as counter electrodes. Celgard 2400 membranes were used as the separators. The electrolyte used here was 1 mol L^{-1} $LiPF_6$ in dimethyl carbonate and ethylene carbonate (1:1 by volume ratio). The active material masses per unit area of Fe_2O_3@MOFC and Fe_2O_3 were 0.64 and 0.65 mg cm^{-2}, respectively. The very close values ensure the accuracy of performance comparison between Fe_2O_3@MOFC and Fe_2O_3. The charge-discharge experiments were performed on a multichannel battery testing system in a voltage window ranging from 0.01 to 3.00 V. Fe_2O_3 and MOFC working electrodes were obtained in the same way.

RESULTS AND DISCUSSION

The overall strategy for production of Fe_2O_3@MOFC is schematically depicted in Scheme 1. Firstly, the particles were synthesized by mixing $FeSO_4 \cdot 7H_2O$ with glycerol in water at 120°C for 24 h. SEM (Fig. 1a, b), TEM (Fig. 1c, d) and synchrotron radiation soft X-ray microscopy images of FeOOH (Fig. S1) indicate that the samples exhibit sea urchin hollow structures with nanoflakes as building units. These building units are about 100 nm in length. The outer diameters of these hollow sea urchin structures are about 900 nm. No peaks from impurities can be found in XRD patterns of these samples (Fig. S2), showing that the product is single-phase FeOOH (JCPDS 29-713).

Secondly, FeOOH nanoparticles were functionalized with MAA. No core-shell structures could be obtained using the unfunctionalized FeOOH nanoparticles, so functionalizing FeOOH with MAA is crucial to the step-by-step assembly. The –SH and –COOH of MAA can bind to the FeOOH and the Fe ions of the MIL-100(Fe) precursor, respectively. The linked Fe ions then react with the organic ligand, thus controlling the growth of the MIL-100(Fe) around the FeOOH [30]. The MAA-functionalized FeOOH was dispersed in $FeCl_3 \cdot 6H_2O$ ethanol solution at 70°C for 15 min and then in H_3BTC ethanol solution at 70°C for 30 min. After ten cycles, the sample was recovered and washed with ethanol, and dried under vacuum at 60°C. The XRD patterns of the as-synthesized samples (Fig. S2) match well with both FeOOH and MIL-100(Fe), even though the intensities of diffraction peaks indexed to MIL-100(Fe) are very weak because the shell is not thick enough. As seen in SEM (Fig. 1e, f) and TEM (Fig. 1g, h) images of the composites, the FeOOH is

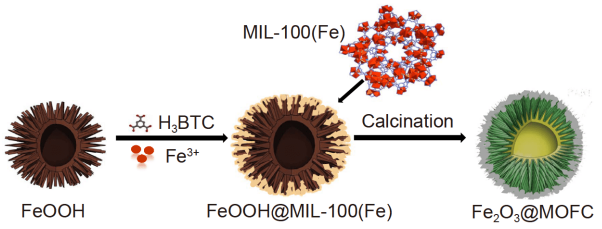

Scheme 1 Illustration of the preparation procedure for hollow sea urchin Fe_2O_3@MOFC nanostructures.

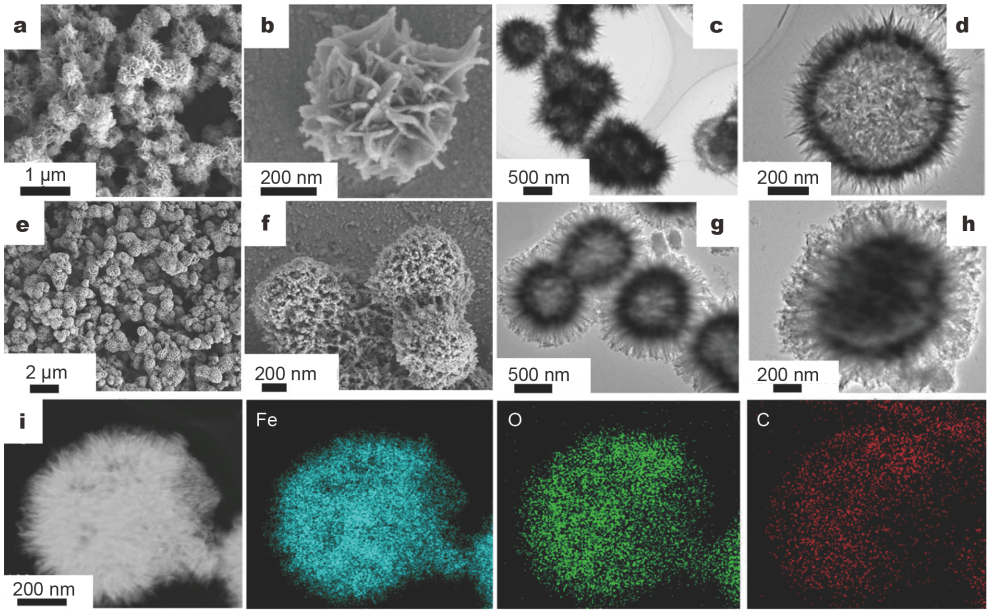

Figure 1 SEM (a, b) and TEM (c, d) images of FeOOH. SEM (e, f) and TEM (g, h) images of FeOOH@MIL-100(Fe). (i) High-angle annular dark-field scanning TEM (HAADF-STEM) images of FeOOH@MIL-100(Fe) and the corresponding elemental mappings for Fe, O and C elements.

homogeneously coated with MIL-100(Fe). Mapping images shown in Fig. 1i clearly reveal that the Fe, O and C elements are homogeneously distributed in the entire architecture, confirming that the FeOOH is uniformly coated with MIL-100(Fe). In order to evaluate the BET surface areas and pore volumes of FeOOH and FeOOH@MIL-100(Fe), BET analysis was performed. As shown in Fig. S3, the FeOOH and FeOOH@MIL-100(Fe) have BET surface areas of 44.40 and 417.23 $m^2 g^{-1}$, respectively. Their pore sizes are about 10 and 2 nm, respectively. The increased surface area of FeOOH@MIL-100(Fe) compared with that of FeOOH was attributed to the outer MOF layer.

Finally, the products were dried and heated at 600°C under N_2 atmosphere for 5 h. Compared with the Fe_2O_3 obtained by calcining FeOOH (Fig. S4a, b), products derived from FeOOH@MIL-100(Fe) maintained the hollow sea urchin morphology after annealing (Fig. S4c, d). XRD were carried out to clarify the structures of the FeO_X@MOFC composites and FeO_X derived from FeOOH@MIL-100(Fe) and FeOOH, respectively. The diffraction peaks shown in Fig. 2a can be ascribed to the characteristic peaks of the cubic phase of maghemite (γ-Fe_2O_3, JCPDS 39-1346). Raman spectra of Fe_2O_3@MOFC (Fig. 2b) display a newly emerged peak at 1600 cm^{-1} compared with Fe_2O_3. This peak can be ascribed to the G band of carbon material, indicating the presence of carbon. Fig. 2c shows the N_2 adsorption-desorption isotherm at 77 K of Fe_2O_3@MOFC. The BET surface area of the Fe_2O_3@MOFC was calculated to be 65.98 $m^2 g^{-1}$. The pore size distribution curve exhibits mesoporous feature of Fe_2O_3@MOFC. The sizes of these pores are about 15 nm. The carbon content is about 3.88% according to thermal gravimetric analysis (TGA) of the Fe_2O_3@MOFC (Fig. S5). The microscopic structures and morphologies of the final composites were further investigated by SEM and TEM. The results are shown in Fig. 3a–d, respectively. Obviously, the morphology of the hollow sea urchin structure could be well preserved during annealing. The high-resolution TEM (HRTEM) image of Fe_2O_3@MOFC is shown in Fig. 3e. Both the outer carbon layer and inner Fe_2O_3 are visible. The carbon layer, which has a thickness of 6–8 nm, is uniform and continuous. The distance between the adjacent planes is 0.28 nm, corresponding to the (211) plane of γ-Fe_2O_3. Weak diffraction rings ascribed to (111), (211), (220), (422) planes in the selected area electron diffraction (SAED) picture (Fig. 3f) further prove that the obtained Fe_2O_3 in

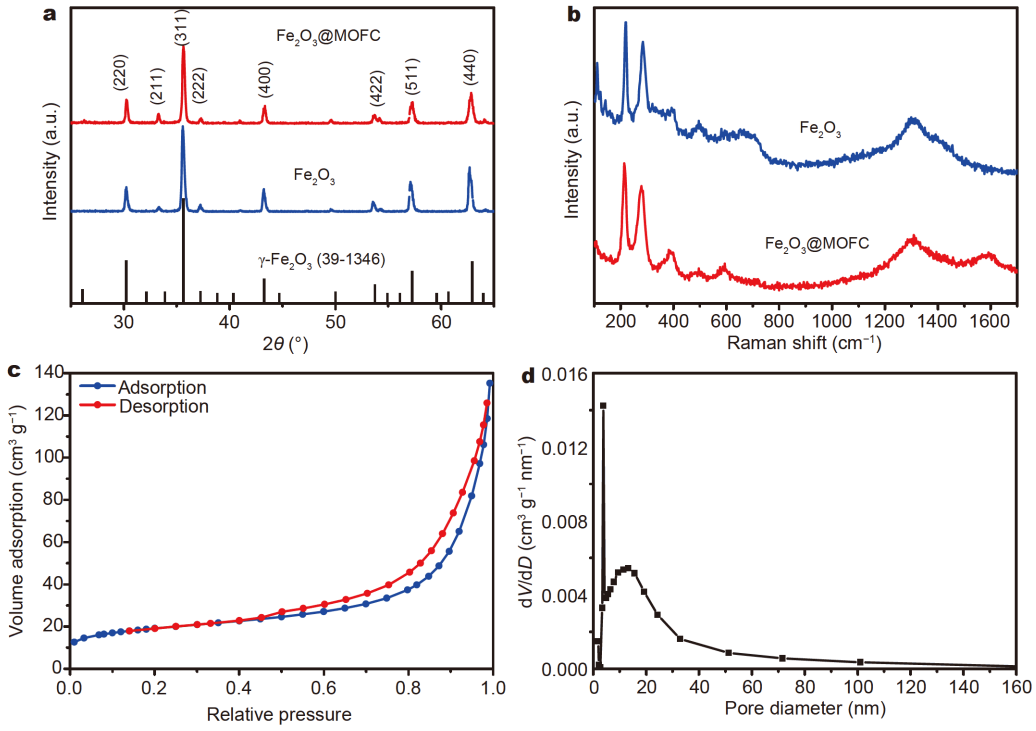

Figure 2 XRD patterns (a) and Raman spectra (b) of Fe_2O_3 and Fe_2O_3@MOFC. N_2 adsorption-desorption isotherm (c) and pore size distribution curve (d) of Fe_2O_3@MOFC.

Fe_2O_3@MOFC is γ-Fe_2O_3, which is consistent with the XRD result. Mapping images (Fig. 3g) indicate that the C, Fe, O elements are homogeneously located throughout the entire architecture.

The chemical states and compositions of the samples were further studied by XPS. As shown in Fig. 4a, two evident peaks at 724.4 and 711.1 eV with a satellite peak at 719.2 eV are observed from Fe 2p spectrum, which matches the fingerprint of the binding energies of Fe_2O_3 [31]. The agreement indicates the presence of Fe_2O_3 in the Fe_2O_3@MOFC composites. The C 1s spectrum illustrated in Fig. 4b can be deconvoluted into four peaks at binding energies of 284.4, 285.1, 285.8 and 287.4 eV, which could be assigned to the sp^2 carbonic, defect-containing sp^2 carbonic, C–O and C=O moieties, respectively, according to previous studies [32]. The O 1s XPS profiles can be fitted with four peaks (Fig. 4c), which are classified as C–O–C (533.3 eV), C=O/C–OH (532.3 eV), C–O–Fe (531.4 eV) and Fe–O (529.7 eV). The signal of C–O–Fe moieties could be observed in both C 1s and

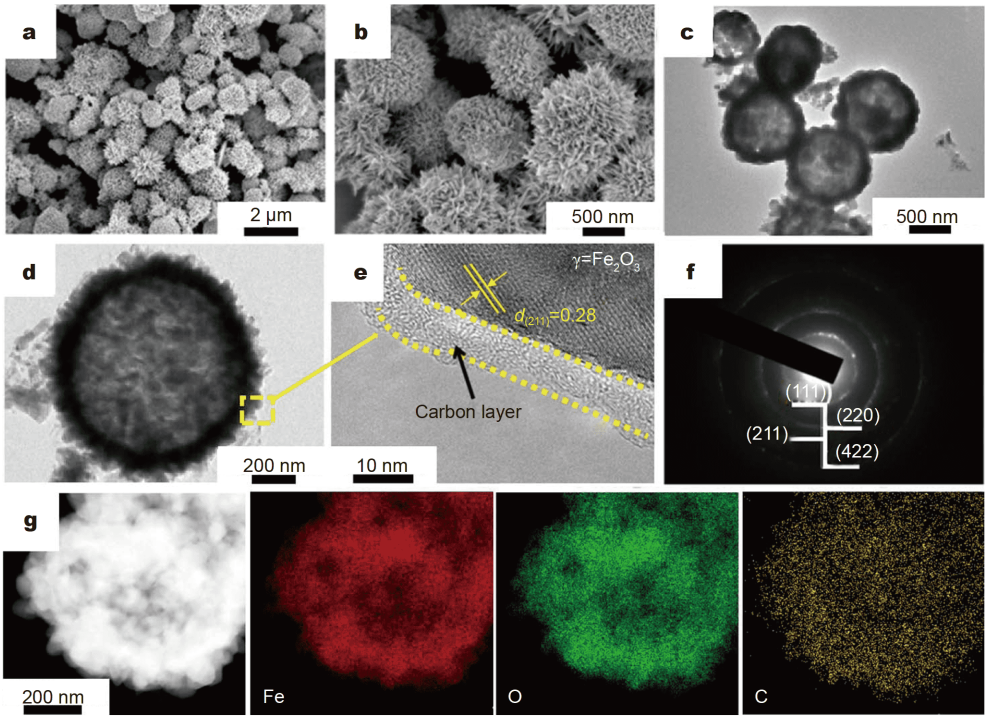

Figure 3 (a, b) SEM images, (c, d) TEM images, (e) HRTEM image, (f) SAED pattern and (g) HAADF-STEM image of Fe_2O_3@MOFC and the corresponding elemental mappings for C, Fe and O elements.

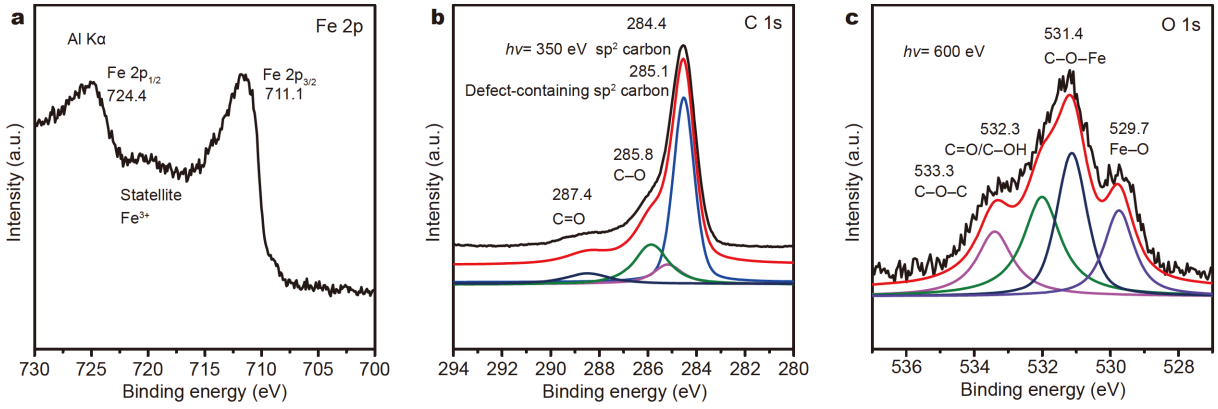

Figure 4 XPS spectra of (a) Fe 2p, (b) C 1s and (c) O 1s of the Fe_2O_3@MOFC.

O 1s spectra, thus further corroborating the linkage of Fe_2O_3 with MOFC through C–O–Fe [33–35].

Promoted by the unique structure of Fe_2O_3@MOFC, it is expected that these composites might be an excellent candidate for LIB anode material [36–38]. The electrochemical properties of Fe_2O_3@MOFC composites, Fe_2O_3 derived from bare FeOOH and MOFC as anode materials are shown in Fig. 5. The charge/discharge profiles of Fe_2O_3@MOFC at 0.1 A g^{-1} with a voltage range of 0.01–3 V are shown in Fig. 5a. In the discharge profile of the first cycle, the voltage drops rapidly from the initial state to 0.85 V and presents a long voltage stage. It can be attributed to the insertion of lithium ions into Fe_2O_3 and the SEI layer formation [39]. Additionally, there is a distinguishable slope from 0.75 to 0.01 V. This may be related to the lithium ion insertion into carbon, reflecting the capacity contribution of carbon composites [40]. During the charge process, the curve first exhibits a smooth rise (0.01–1.5 V), followed by a tilted voltage platform (1.5–1.8 V) and ends with a steep rise (1.8–3.0 V). The tilted voltage platform corresponds to the oxidation of metallic Fe to Fe_2O_3. At the first cycle, the hybrids deliver specific discharge and charge capacities of 1366.9 and 917.5 mA h g^{-1}, respectively, with a Coulombic efficiency of 67%. The 33% irreversible capacity loss is attributed to electrolyte decomposition and the formation of SEI film [41]. However, the Coulombic efficiency of the 2nd cycle increases to 97.8% and remains almost 100% in the following cycles (the black curve in Fig. 5b). The voltage platform at 0.1 V, which typically belongs to carbon materials [42], does not show up from all curves in Fig. 5a, indicating that the capacity contribution of MOFC is rather small. It is seen that the slope at the end of charge curves decreases gradually with the increase of cycle numbers from 2, 50, to 100, suggesting an obvious capacitance behavior [43].

To further quantify the capacitive contribution to the total capacity of the electrode, a method proposed by Chen *et al.* [44] and Brezesinski *et al.* [45] was adopted. The current response at a certain potential can be separated into two parts: pseudocapacitive effects (k_1v) and diffusion-controlled Li^+ insertion/extraction ($k_2v^{1/2}$). The calculation formula is [45,46]:

$$i(V)=k_1v+k_2v^{1/2}. \quad (1)$$

The Equation (1) can be changed to:

$$i(V)/v^{1/2}=k_1v^{1/2}+k_2. \quad (2)$$

The coefficients k_1 and k_2 can be determined by the linear fitting of voltammetric currents at each potential [45]. As shown in Fig. 6a–e, the shadowed areas represent the contribution from the surface capacitive current, and the blank regions stand for the diffusion-controlled cur-

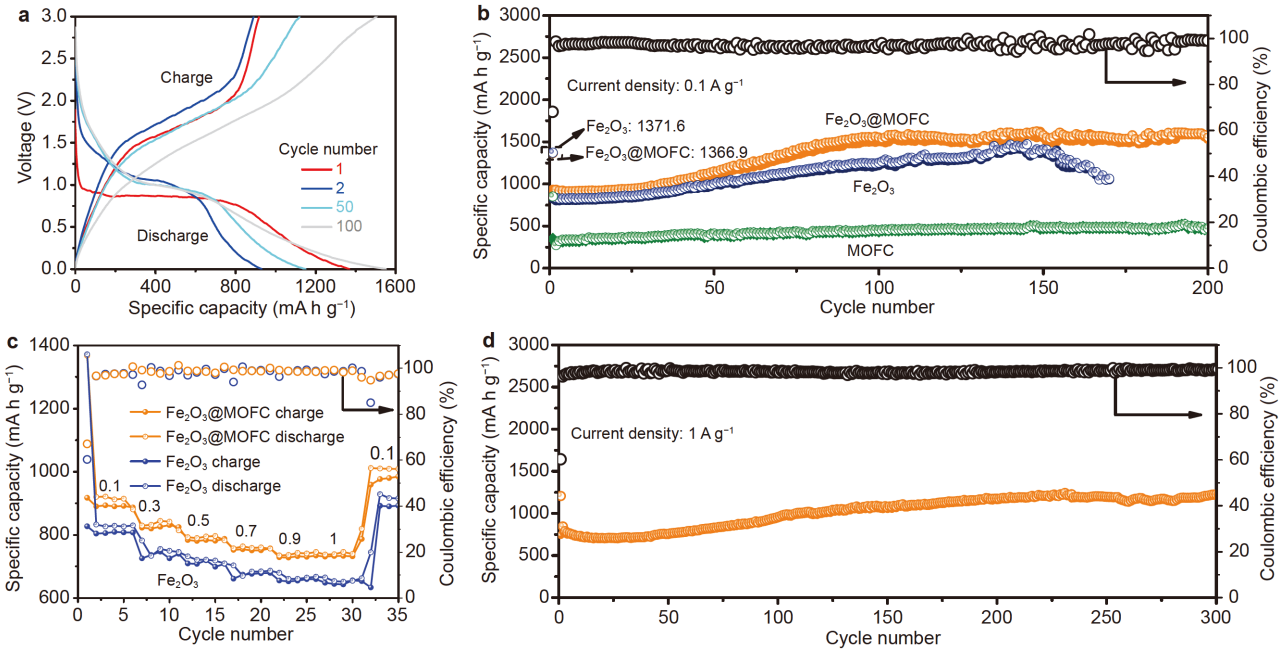

Figure 5 (a) Discharge/charge voltage profiles of Fe_2O_3@MOFC. (b) Comparative cycling performances of Fe_2O_3@MOFC, Fe_2O_3, and MOFC. In these tests, the discharge/charge cycling curves were taken between 0.01 and 3.0 V at a current density of 0.1 A g^{-1}. (c) Rate capacities of Fe_2O_3@MOFC and Fe_2O_3 at various current densities ranging from 0.1 to 1 A g^{-1}. (d) Cycling performance of Fe_2O_3@MOFC at a current density of 1 A g^{-1}.

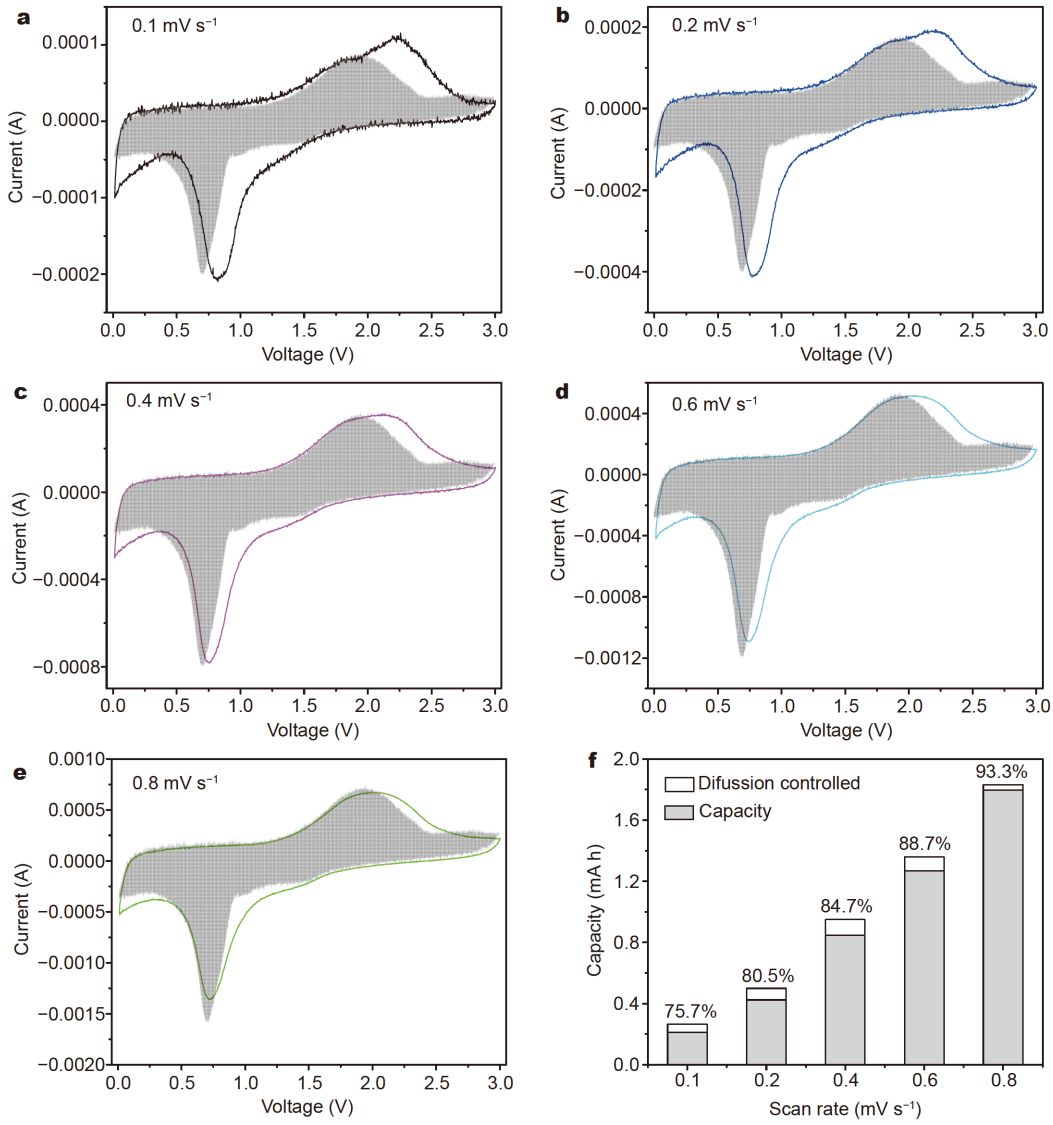

Figure 6 Cyclic voltammetry of Fe_2O_3@MOFC tested *vs.* Li/Li^+ at (a) 0.1, (b) 0.2, (c) 0.4, (d) 0.6 and (e) 0.8 mV s^{-1}. The shadowed regions stand for the capacitive contribution. (f) Separation of diffusion-controlled and capacitive charge at various sweep rates. The shadowed areas represent the contribution from the surface capacitive current, and the blank regions stand for the diffusion-controlled current contribution.

rent contribution. At 0.1 mV s^{-1}, the capacitive-controlled capacity constitutes 75.7% of the total capacity (Fig. 6a), while this ratio rises to 93.3% at 0.8 mV s^{-1} (Fig. 6e). Contributions of the two different mechanisms at other scan rates were also quantified (Fig. 6b–d). Fig. 6f shows the quantified result, which indicates that the capacitive capacity improves gradually with increasing scan rate.

Fig. 5b shows the galvanostatic cycling performances of Fe_2O_3, MOFC and Fe_2O_3@MOFC composites. It is found that the specific capacity of Fe_2O_3@MOFC is much larger than those of Fe_2O_3 and MOFC. In addition, the specific capacity of Fe_2O_3@MOFC increases initially and then becomes almost steady to 1551.3 mA h g^{-1} along with the increase of cycling numbers. For the Fe_2O_3 electrode, the capacity decays much faster after 150 cycles. The larger specific capacity and better stability of Fe_2O_3@MOFC can be attributed to the MOF-derived carbon coating layer. It seals Fe_2O_3 inside thoroughly from the morphological perspective and possesses strong chemical bonding between Fe_2O_3 and the coating layer, as proved by the XPS measurements. As a result, these protective effects prevent the internal Fe_2O_3 from volume expansion during cycling, thus improving the cycling performance. In addition, the outer carbon layer can hinder the direct con-

tact between Fe_2O_3 and the electrolyte, thereby reducing the formation of SEI, resulting in a high Coulombic efficiency of Fe_2O_3@MOFC [15]. As shown in the electrochemical impendence spectroscopy (EIS) patterns of Fe_2O_3@MOFC, Fe_2O_3 and MOFC (Fig. S6), both Fe_2O_3@MOFC and MOFC show lower resistance than Fe_2O_3, according to the decreased diameter of the semicircle at the high-frequency region and the obviously steep slope line at the low-frequency region. Therefore, carbon coating can reduce the charge transfer resistance of the composites, which enhances the electrical conductivity and Li^+ diffusion [13,14].

The rate performance of the Fe_2O_3@MOFC electrode was evaluated at the current densities from 0.1 to 1 A g^{-1}. Fig. 5c presents the capacities of Fe_2O_3@MOFC and Fe_2O_3 at different current densities including 0.1, 0.3, 0.5, 0.7, 0.9 and 1 A g^{-1}. The corresponding reversible specific capacity values of Fe_2O_3@MOFC reach 917, 845, 798, 764, 742 and 741 mA h g^{-1}, respectively. Once the rate is lowered back to 0.1 A g^{-1}, a high rate capacity of 972 mA h g^{-1} can be recovered, showing an excellent rate performance. At all current densities, the Coulombic efficiencies of Fe_2O_3@MOFC are more stable than those of Fe_2O_3, indicating the better rate performance of Fe_2O_3@MOFC.

The cycling performance and the Coulombic efficiency of the Fe_2O_3@MOFC composites were also tested at a current density of 1 A g^{-1}, as illustrated in Fig. 5d. As can be seen, the Fe_2O_3@MOFC electrode delivers a high specific capacity of 1248.5 mA h g^{-1} in the first cycle. Afterwards, it goes through a slight fading down region, and the specific capacity gradually decreases to 740.6 mA h g^{-1} after 35 cycles. Interestingly, in the range of 35–220 cycles, the capacity exhibits a steady rising state and stabilizes at 1208.6 mA h g^{-1} and keeps this level up to 300 cycles. In addition, the Coulombic efficiency maintains almost consistently at around 100% throughout the whole process.

For comparison purposes, the advanced LIB anode materials and their characteristics are summarized in Table S1. In addition, the electrochemical properties of Fe_2O_3@MOFC composites in this work and other Fe_2O_3-based anode materials ever reported are also summarized in Table S2. The results show that the Fe_2O_3@MOFC composites possess excellent electrochemical properties in terms of high reversible capacity and good cycling stability. It should be mentioned that such a capacity rise during charge/discharge process also appeared in some other nanostructured metal oxide anode materials [47–49]. To investigate the behavior of specific capacity increase of lithium storage in the Fe_2O_3@MOFC structures, the differential capacity *versus* voltage curves of various cycles were measured. The results are shown in Fig. 7. In order to understand these curves, it is necessary to mention the reaction mechanism during the charge/discharge process. According to previous studies [7,50,51], the reaction steps during the charge/discharge process can be described as follows:

$$Fe_2O_3+xLi^++xe^-\rightarrow Li_xFe_2O_3, \quad (3)$$

$$Li_xFe_2O_3+(2-x)Li^++(2-x)e^-\rightarrow Li_2Fe_2O_3, \quad (4)$$

$$Li_2Fe_2O_3+4Li^++4e^-\rightarrow 2Fe^0+3Li_2O. \quad (5)$$

The first two reactions are mainly irreversible. The last reaction is largely reversible. Therefore the total reversible reaction is:

$$Fe_2O_3+6Li^++6e^-\leftrightarrow 2Fe+3Li_2O. \quad (6)$$

In Fig. 7, in the 1st cycle, three peaks at 1.34, 1.05 and 0.88 V can be observed, corresponding to the formation of $Li_xFe_2O_3$ (reaction (1)), the transition from $Li_xFe_2O_3$ to $Li_2Fe_2O_3$ (reaction (2)) and the formation of SEI film, respectively. The wide peak from 1.4 to 2.0 V corresponds to the recovery of Fe^0 to $Li_2Fe_2O_3$ (reaction (3)). The repeatable cathodic and anodic peak pair at around 1.0 and 1.4–2.0 V of subsequent curves indicate reversible conversion between $Li_2Fe_2O_3$ and Fe^0. The initial peaks at 1.34 and 0.88 V disappear, because the phase transition from $Li_xFe_2O_3$ to $Li_2Fe_2O_3$ and SEI film formation are irreversible. The peak intensities around 1.00 V of 50th and 100th cycles are much stronger than that of the 1st cycle, corresponding to the enhanced reversibility of the conversion reaction between $Li_2Fe_2O_3$ and Fe^0 for lithium storage, which may induce the capacity increase.

The Fe_2O_3@MOFC anode materials were further in-

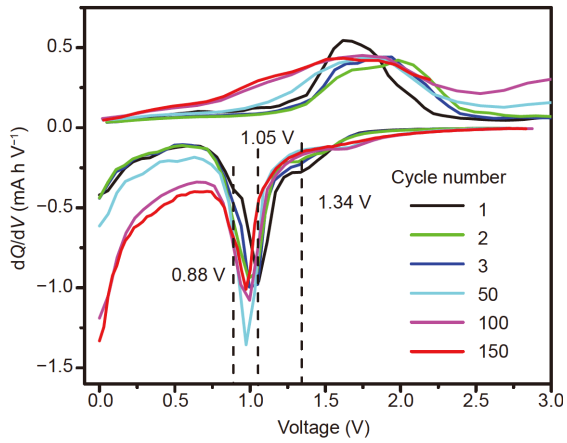

Figure 7 The differential capacity *versus* voltage plots of the Fe_2O_3@MOFC composites at selected cycle numbers.

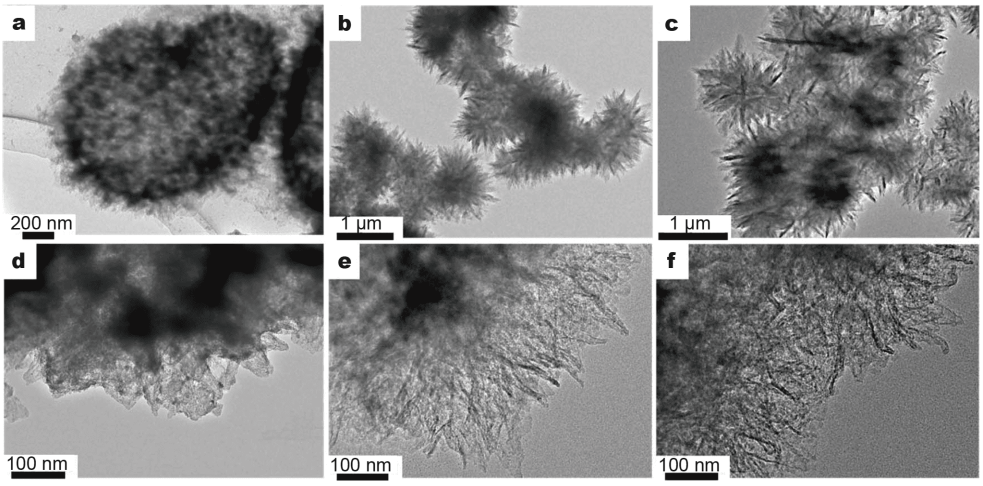

Figure 8 TEM images of the Fe_2O_3@MOFC composites after 50 (a, d), 100 (b, e), 150 (c, f) discharge/charge cycles at 0.1 A g^{-1}.

vestigated by TEM after several discharge/charge cycles. Fig. 8 shows the TEM images of Fe_2O_3@MOFC composites after 50, 100 and 150 discharge/charge cycles at 0.1 A g^{-1}. Compared with the morphology of the pristine Fe_2O_3@MOFC (Fig. 3c, d), the nanoflakes of Fe_2O_3@MOFC composites grow up after 50 (Fig. 8a, d) and 100 discharge/charge cycles (Fig. 8b, e). The growing nanoflakes may increase the electrode/electrolyte contact area, thus facilitating the insertion/extraction of lithium ions and enhancing the pseudocapacitance behavior [52]. The Fe_2O_3@MOFC composites after 150 (Fig. 8c, f) discharge/charge cycles exhibit similar morphologies, corresponding to steady cycling performance between the 100th to 150th cycles in Fig. 5b. In addition, some polymeric gel-like films seem to be formed on the nanoparticles during the discharge/charge cycles. The well-maintained integrity and stability of Fe_2O_3@MOFC guarantee the excellent electrochemical stability of the electrode.

Overall, several factors might cause the increased specific capacity. First, the enhanced reversibility of the conversion reaction between $Li_2Fe_2O_3$ and Fe^0 for lithium storage may induce capacity increase. Second, the growing nanoflakes could increase the electrode/electrolyte contact area, which may facilitate the insertion/extraction of Li^+ and enhance the pseudocapacitance behavior. Third, it may be due to the activation process [36,53]. It is conjectured that the Fe_2O_3@MOFC electrode is rearranged during cycling. Therefore, the irreversible Li_2O formed during early cycles could be re-exposed and thus participate in the electrochemical reaction [54]. The existence of carbon materials could even enhance the active process [55]. In addition, the delayed wetting of the electrolyte into the electrode may also contribute to the increase of specific capacity [36].

CONCLUSIONS

In summary, a concise and controllable method for the synthesis of hollow sea urchin nanostructured Fe_2O_3 coated by carbon (Fe_2O_3@MOFC) has been developed. FeOOH@MIL-100(Fe) was used as the sacrificial template and precursor. The outer MOF layer protects the integrity of inner Fe_2O_3 during the thermolysis process. Benefitting from the unique nanostructure and *in-situ* constructed carbon layer on the surface of Fe_2O_3, the Fe_2O_3@MOFC composites exhibit enhanced cycling performance (1551.3 mA h g^{-1} after 200 cycles at 0.1 A g^{-1} and 1208.6 mA h g^{-1} after 300 cycles at 1 A g^{-1}) and excellent rate performance. The results presented here give clear evidences that MOF-derived carbon coatings and unique structure can improve the electrochemical performance of nanostructured TMOs applied in LIBs. The approach for the synthesis of TMOs@MOFC here suggests a new method to fabricate various nanostructured TMO@-carbon composites used in electrochemical energy storage devices.

Received 17 April 2020; accepted 23 June 2020; published online 25 August 2020

1 Li Y, Zhou W, Xin S, *et al.* Fluorine-doped antiperovskite electrolyte for all-solid-state lithium-ion batteries. Angew Chem Int Ed, 2016, 55: 9965–9968
2 Dong X, Chen L, Liu J, *et al.* Environmentally-friendly aqueous Li (or Na)-ion battery with fast electrode kinetics and super-long life. Sci Adv, 2016, 2: e1501038
3 Huang M, Mi K, Zhang J, *et al.* MOF-derived bi-metal embedded N-doped carbon polyhedral nanocages with enhanced lithium storage. J Mater Chem A, 2017, 5: 266–274

4 Chaudhari S, Srinivasan M. 1D hollow α-Fe_2O_3 electrospun nanofibers as high performance anode material for lithium ion batteries. J Mater Chem, 2012, 22: 23049–23056
5 Cherian CT, Sundaramurthy J, Kalaivani M, *et al.* Electrospun α-Fe_2O_3 nanorods as a stable, high capacity anode material for Li-ion batteries. J Mater Chem, 2012, 22: 12198–12204
6 Sahay R, Suresh Kumar P, Aravindan V, *et al.* High aspect ratio electrospun CuO nanofibers as anode material for lithium-ion batteries with superior cycleability. J Phys Chem C, 2012, 116: 18087–18092
7 Wang Z, Luan D, Madhavi S, *et al.* Assembling carbon-coated α-Fe_2O_3 hollow nanohorns on the CNT backbone for superior lithium storage capability. Energy Environ Sci, 2012, 5: 5252–5256
8 Wu ZS, Zhou G, Yin LC, *et al.* Graphene/metal oxide composite electrode materials for energy storage. Nano Energy, 2012, 1: 107–131
9 Zhang L, Wu HB, Madhavi S, *et al.* Formation of Fe_2O_3 microboxes with hierarchical shell structures from metal–organic frameworks and their lithium storage properties. J Am Chem Soc, 2012, 134: 17388–17391
10 Wang Z, Zhou L, David Lou XW. Metal oxide hollow nanostructures for lithium-ion batteries. Adv Mater, 2012, 24: 1903–1911
11 Xiao L, Wu D, Han S, *et al.* Self-assembled Fe_2O_3/graphene aerogel with high lithium storage performance. ACS Appl Mater Interfaces, 2013, 5: 3764–3769
12 Wang R, Xu C, Sun J, *et al.* Three-dimensional Fe_2O_3 nanocubes/nitrogen-doped graphene aerogels: Nucleation mechanism and lithium storage properties. Sci Rep, 2014, 4: 7171
13 Sun LY, Yang L, Li J, *et al.* Superior full-cell cycling and rate performance achieved by carbon coated hollow Fe_3O_4 nanoellipsoids for lithium ion battery. Electrochim Acta, 2018, 288: 71–81
14 Ding R, Zhang J, Qi J, *et al.* N-doped dual carbon-confined 3D architecture rGO/Fe_3O_4/AC nanocomposite for high-performance lithium-ion batteries. ACS Appl Mater Interfaces, 2018, 10: 13470–13478
15 Agyeman DA, Song K, Lee GH, *et al.* Carbon-coated Si nanoparticles anchored between reduced graphene oxides as an extremely reversible anode material for high energy-density Li-ion battery. Adv Energy Mater, 2016, 6: 1600904
16 Lu X, Dong S, Chen Z, *et al.* Preparation of carbon coated $Ti_2Nb_2O_9$ nanosheets and its sodium ion storage properties. Acta Phys-Chim Sin, 2020, 36: 1906024
17 Chen X, Li H, Yan Z, *et al.* Structure design and mechanism analysis of silicon anode for lithium-ion batteries. Sci China Mater, 2019, 62: 1515–1536
18 Cui Y, Li B, He H, *et al.* Metal–organic frameworks as platforms for functional materials. Acc Chem Res, 2016, 49: 483–493
19 Yuan S, Feng L, Wang K, *et al.* Stable metal-organic frameworks: Design, synthesis, and applications. Adv Mater, 2018, 30: 1704303
20 Yang L, Zeng X, Wang W, *et al.* Recent progress in MOF-derived, heteroatom-doped porous carbons as highly efficient electrocatalysts for oxygen reduction reaction in fuel cells. Adv Funct Mater, 2018, 28: 1704537
21 Cao X, Zheng B, Rui X, *et al.* Metal oxide-coated three-dimensional graphene prepared by the use of metal-organic frameworks as precursors. Angew Chem Int Ed, 2014, 53: 1404–1409
22 Zhao M, Yuan K, Wang Y, *et al.* Metal–organic frameworks as selectivity regulators for hydrogenation reactions. Nature, 2016, 539: 76–80
23 Simon-Yarza T, Mielcarek A, Couvreur P, *et al.* Nanoparticles of metal-organic frameworks: On the road to *in vivo* efficacy in biomedicine. Adv Mater, 2018, 30: 1707365
24 Szczęśniak B, Choma J, Jaroniec M. Gas adsorption properties of hybrid graphene-MOF materials. J Colloid Interface Sci, 2018, 514: 801–813
25 Howarth AJ, Katz MJ, Wang TC, *et al.* High efficiency adsorption and removal of selenate and selenite from water using metal–organic frameworks. J Am Chem Soc, 2015, 137: 7488–7494
26 Song Y, Li X, Sun L, *et al.* Metal/metal oxide nanostructures derived from metal–organic frameworks. RSC Adv, 2015, 5: 7267–7279
27 Yi M, Zhang C, Cao C, *et al.* MOF-derived hybrid hollow submicrospheres of nitrogen-doped carbon-encapsulated bimetallic Ni–Co–S nanoparticles for supercapacitors and lithium ion batteries. Inorg Chem, 2019, 58: 3916–3924
28 Hou L, Jiang X, Jiang Y, *et al.* Facile preparation of porous rod-like $Cu_xCo_{3-x}O_4$/C composites *via* bimetal–organic framework derivation as superior anodes for lithium-ion batteries. ACS Omega, 2019, 4: 7565–7573
29 Wang K, Chen M, He Z, *et al.* Hierarchical Fe_3O_4@C nanospheres derived from Fe_2O_3/MIL-100(Fe) with superior high-rate lithium storage performance. J Alloys Compd, 2018, 755: 154–162
30 Ke F, Qiu LG, Yuan YP, *et al.* Fe_3O_4@MOF core–shell magnetic microspheres with a designable metal–organic framework shell. J Mater Chem, 2012, 22: 9497–9500
31 Descostes M, Mercier F, Thromat N, *et al.* Metal oxide-coated three-dimensional graphene prepared by the use of metal-organic frameworks as precursors. Appl Surf Sci, 2000, 165: 288–302
32 Bhadra BN, Yoo DK, Jhung SH. Carbon-derived from metal-organic framework MOF-74: A remarkable adsorbent to remove a wide range of contaminants of emerging concern from water. Appl Surf Sci, 2020, 504: 144348
33 Zhou J, Song H, Ma L, *et al.* Magnetite/graphene nanosheet composites: interfacial interaction and its impact on the durable high-rate performance in lithium-ion batteries. RSC Adv, 2011, 1: 782–791
34 Li L, Zhou G, Weng Z, *et al.* Monolithic Fe_2O_3/graphene hybrid for highly efficient lithium storage and arsenic removal. Carbon, 2014, 67: 500–507
35 Zhou H, Liu C, Wu JC, *et al.* Boosting the electrochemical performance through proton transfer for the Zn-ion hybrid supercapacitor with both ionic liquid and organic electrolytes. J Mater Chem A, 2019, 7: 9708–9715
36 Cao K, Jiao L, Liu H, *et al.* 3D hierarchical porous α-Fe_2O_3 nanosheets for high-performance lithium-ion batteries. Adv Energy Mater, 2015, 5: 1401421
37 Ge X, Liu S, Qiao M, *et al.* Enabling superior electrochemical properties for highly efficient potassium storage by impregnating ultrafine Sb nanocrystals within nanochannel-containing carbon nanofibers. Angew Chem Int Ed, 2019, 58: 14578–14583
38 Tu F, Han Y, Du Y, *et al.* Hierarchical nanospheres constructed by ultrathin MoS_2 nanosheets braced on nitrogen-doped carbon polyhedra for efficient lithium and sodium storage. ACS Appl Mater Interfaces, 2019, 11: 2112–2119
39 Li Y, Zhu C, Lu T, *et al.* Simple fabrication of a Fe_2O_3/carbon composite for use in a high-performance lithium ion battery. Carbon, 2013, 52: 565–573
40 Xia H, Zhu D, Fu Y, *et al.* $CoFe_2O_4$-graphene nanocomposite as a high-capacity anode material for lithium-ion batteries. Electrochim Acta, 2012, 83: 166–174

41 Li X, Meng X, Liu J, *et al.* Tin oxide with controlled morphology and crystallinity by atomic layer deposition onto graphene nanosheets for enhanced lithium storage. Adv Funct Mater, 2012, 22: 1647–1654
42 Yoo EJ, Kim J, Hosono E, *et al.* Large reversible Li storage of graphene nanosheet families for use in rechargeable lithium ion batteries. Nano Lett, 2008, 8: 2277–2282
43 Xu D, Li B, Wei C, *et al.* Preparation and characterization of MnO_2/acid-treated CNT nanocomposites for energy storage with zinc ions. Electrochim Acta, 2014, 133: 254–261
44 Chen C, Wen Y, Hu X, *et al.* Na^+ intercalation pseudocapacitance in graphene-coupled titanium oxide enabling ultra-fast sodium storage and long-term cycling. Nat Commun, 2015, 6: 6929
45 Brezesinski K, Wang J, Haetge J, *et al.* Pseudocapacitive contributions to charge storage in highly ordered mesoporous group V transition metal oxides with iso-oriented layered nanocrystalline domains. J Am Chem Soc, 2010, 132: 6982–6990
46 Wang R, Lang J, Zhang P, *et al.* Fast and large lithium storage in 3D porous VN nanowires-graphene composite as a superior anode toward high-performance hybrid supercapacitors. Adv Funct Mater, 2015, 25: 2270–2278
47 Lian P, Zhu X, Liang S, *et al.* High reversible capacity of SnO_2/graphene nanocomposite as an anode material for lithium-ion batteries. Electrochim Acta, 2011, 56: 4532–4539
48 Su Y, Li S, Wu D, *et al.* Two-dimensional carbon-coated graphene/metal oxide hybrids for enhanced lithium storage. ACS Nano, 2012, 6: 8349–8356
49 Laruelle S, Grugeon S, Poizot P, *et al.* On the origin of the extra electrochemical capacity displayed by MO/Li cells at low potential. J Electrochem Soc, 2002, 149: A627
50 Larcher D, Masquelier C, Bonnin D, *et al.* Effect of particle size on lithium intercalation into α-Fe_2O_3. J Electrochem Soc, 2003, 150: A133
51 Larcher D, Bonnin D, Cortes R, *et al.* Combined XRD, EXAFS, and Mossbauer studies of the reduction by lithium of α-Fe_2O_3 with various particle sizes. J Electrochem Soc, 2003, 150: A1643
52 Lee SH, Yu SH, Lee JE, *et al.* Self-assembled Fe_3O_4 nanoparticle clusters as high-performance anodes for lithium ion batteries *via* geometric confinement. Nano Lett, 2013, 13: 4249–4256
53 Gao G, Zhang Q, Wang K, *et al.* Axial compressive α-Fe_2O_3 microdisks prepared from CSS template for potential anode materials of lithium ion batteries. Nano Energy, 2013, 2: 1010–1018
54 Guo W, Sun W, Lv LP, *et al.* Microwave-assisted morphology evolution of Fe-based metal–organic frameworks and their derived Fe_2O_3 nanostructures for Li-ion storage. ACS Nano, 2017, 11: 4198–4205
55 Zhu T, Chen JS, Lou XWD. Glucose-assisted one-pot synthesis of FeOOH nanorods and their transformation to Fe_3O_4@carbon nanorods for application in lithium ion batteries. J Phys Chem C, 2011, 115: 9814–9820

Acknowledgements This work was financially supported by the National Key R&D Program of China (2017YFA0403402 and 2019YFA0405601), the National Natural Science Foundation of China (21773222, U1732272 and U1932214), the DNL Cooperation Fund, and Chinese Academy of Sciences (DNL180201).

Author contributions Feng Y designed and engineered the samples; Shu N and Xie J performed the electrochemical experiments; Feng Y wrote the paper with support from Zhu J, Ke F and Zhu Y. All authors contributed to the general discussion.

Conflict of interest The authors declare that they have no conflict of interest.

Supplementary information Experimental details and supporting data are available in the online version of the paper.

Yuge Feng is a PhD student at the National Synchrotron Radiation Laboratory, University of Science and Technology of China (USTC). Her research interests mainly focus on synthesis and characterization of metal-organic frameworks (MOFs) for energy applications.

Junfa Zhu received his PhD in physical chemistry from USTC in 1999. After several years working in the Institute of Experimental Physics, Johannes-Kepler-Universität Linz (Austria), Lehrstuhl für Physikalische Chemie II, Friedrich-Alexander-Universität Erlangen-Nürnberg (Germany), Department of Chemistry, University of Washington (USA), he returned to USTC in December, 2006, and became a professor at the National Synchrotron Radiation Laboratory, USTC under the support of "Hundred Talent Program" of Chinese Academy of Sciences. His research interests mainly focus on *in-situ* studies of surface chemistry and catalysis, surface/interface structures and properties of functional materials, and surface coordination chemistry.

中空海胆状结构的碳包覆Fe_2O_3用作锂离子电池的高性能负极材料

冯雨歌[1], 束娜[2], 谢兼[2], 柯飞[3], 朱彦武[2], 朱俊发[1*]

摘要 Fe_2O_3由于成本低廉，储量丰富和理论比容量高(1007 mA h g^{-1})等特点，在锂离子电池负极材料的应用中极具发展前景. 然而一些问题仍然存在，如：充放电过程中比容量的迅速衰减，不可逆的体积膨胀以及较短的循环寿命等. 这些问题严重制约了Fe_2O_3在锂离子电池中的实际应用. 为了突破这些局限，本文以金属-有机骨架(MOFs)包覆的FeOOH(FeOOH@MIL-100(Fe))作为前驱体和自牺牲模板，通过高温热处理制备得到一种能良好继承前驱体形貌的中空海胆状碳包覆的Fe_2O_3(Fe_2O_3@MOFC)复合材料. 在热处理过程中，外部的MOF层很好地保护了内部Fe_2O_3结构的完整性，并以原位转化的方式衍生为均匀分布在纳米粒子外部的碳涂层. 在 0.1 A g^{-1} 的电流密度下，Fe_2O_3@MOFC可提供高达1366.9 mA h g^{-1}的初始放电容量，且充放电循环200次后，仍能保持大约1551.3 mA h g^{-1}的高放电容量. 在1 A g^{-1}的高电流密度下循环300次后，其比容量仍可保持在1208.6 mA h g^{-1}.

